

Research Article

Laboratory Study on the Effect of Fluid Pressurization Rate on Fracture Instability

Xinyao Wang ¹, Quanchen Gao ¹, Xiao Li ², and Dianzhu Liu ¹

¹School of Mechanics and Civil Engineering, China University of Mining and Technology (Beijing), Beijing 100083, China

²Key Laboratory of Shale Gas and Geoengineering, Institute of Geology and Geophysics, Chinese Academy of Sciences, Beijing 100029, China

Correspondence should be addressed to Xinyao Wang; lnwangxinyao@126.com

Received 5 April 2021; Accepted 20 May 2021; Published 9 June 2021

Academic Editor: Yu Wang

Copyright © 2021 Xinyao Wang et al. This is an open access article distributed under the Creative Commons Attribution License, which permits unrestricted use, distribution, and reproduction in any medium, provided the original work is properly cited.

Fluid injection-induced earthquakes have been a scientific and social issue of wide concern, and fluid pressurization rate may be an important inducement. Therefore, a series of stepwise and conventional injection-induced shear tests were carried out under different fluid pressurization rates and effective normal stresses. The results show that the magnitude of fluid pressure is the main factor controlling the initiation of fracture slipping. The contribution of fluid pressure heterogeneity and permeability evolution on the initiation of fracture slipping is different with the increase of fluid pressurization rate. When the fluid pressurization rate is small, permeability evolution plays a dominant role. On the contrary, the fluid pressure heterogeneity plays a dominant role. The increase of fluid pressurization rate may lead to the transition from creep slip mode to slow stick-slip mode. Under the laboratory scale, the fluid pressure heterogeneity causes the coulomb failure stress to increase by about one times than the predicted value at the initiation of fracture slipping, and the coulomb stress increment threshold of 1.65 MPa is disadvantageous to the fracture stability.

1. Introduction

In the last 10 years, the worldwide exponential increase of fluid injection-induced earthquakes has become a widely concerned scientific and social problem. This is due to hydraulic fracturing, enhanced geothermal stimulation, and saltwater disposal engineering operations which result in the reactivation of faults [1]. However, the role of fluid injection procedures in induced earthquakes remains controversial, and the key knowledge gaps in risk management remain. Understanding the mechanism by which fluid injection procedures induced fault slip is important for improving seismic risk associated with large-scale fluid injection.

According to the effective stress principle and Mohr-Coulomb failure criterion, fault instability occurs when the shear stress on a rock fracture exceeds the product of the friction coefficient and effective normal stress, which is given by the difference between the normal stress and fluid pressure. Elevating the fluid pressure during fluid injection decreases the effective normal stress, resulting in fault instability [2–

6]. However, this is restricted to fault slip initiation caused by fluid overpressure. Recent studies showed that fluid overpressure is not the only parameter governing fault reactivation and the associated seismicity. The fluid pressurization rate and the fluid pressure heterogeneity are also closely related to the fault slip initiation and slip mode [7]. French et al. performed axial compression and lateral relaxation tests on permeable sandstones with saw-cut surfaces. Fluid injection into a saw-cut granite sample in stress relaxation test shows that the onset of fault activation may not be predicted by the principle of effective stress at high injection rates [8]. This is presumably caused by a significantly heterogeneous distribution of fluid pressure on the fault plane [9, 10]. In addition, the influence of permeability evolution on fracture slip has also been concerned, and it has been regarded as a supplementary mechanism of fluid injection induced fault slip. However, the physical mechanisms controlling fault slip initiation and slip mode in response to fluid pressurization are still a matter of debate. The mismatch between seismic time and fluid injection time is still not clear.

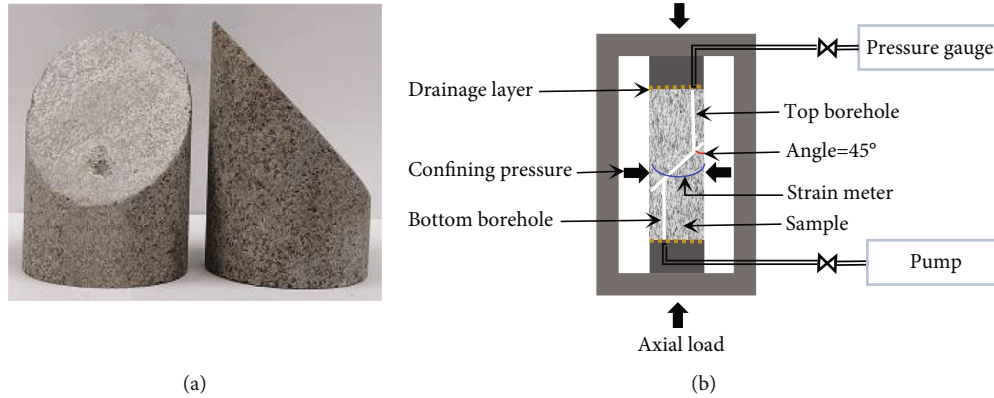


FIGURE 1: Experimental material and configuration. (a) Saw-cut sandstone fracture. (b) Sketch of sample assembly installed inside the triaxial pressure vessel.

The objective of this study is to unravel the slip characteristics of a critically stressed fracture associated with fluid pressurization rate. We conducted injection-induced fracture slip experiments on saw-cut permeable sandstones using different fluid injection schemes. The influence of fluid pressurization rate on fracture slip mode and displacement evolution process under different fluid injection rates is compared and analyzed. In addition, we also analyzed the influence of fluid pressure heterogeneity and permeability evolution on fracture slip initiation.

2. Experimental Configuration and Method

2.1. Experimental Material and Configuration. The cylindrical samples of sandstone of 50 mm in diameter were cored and then cut and precisely ground to a length of 100 mm. The sample was then cut at 45° with respect to its axis to create an elliptical saw cut fracture interface of 50 mm in width and 70 mm in length along strike (Figure 1(a)). The fracture surfaces were then polished using sandpaper with $300\ \mu\text{m}$ particle size. Two 3 mm diameter boreholes were drilled parallel to the core axis at the sample ends to maximize the fluid diffusion distance along the fracture. The fractured sample was placed in two heat shrinkable tubes and equipped with axial and radial extensometers (Figure 1(b)). The tests were carried out using the TAW-2000 electrohydraulic servo rock triaxial testing machine, from Key Laboratory of Shale Gas and Geological Engineering, Institute of Geology and Geophysics, Chinese Academy of Sciences at ambient temperature (25°C). The testing machine has an independent closed-loop control system of axial pressure, confining pressure, and pore water pressure. The range of axial pressure is 0-2000 kN, confining pressure is 0-100 MPa, and pore water pressure is 0-60 MPa. The whole process test of uniaxial and triaxial strain, cyclic loading, and other tests with the diameter of the specimen ranging from 25 mm to 100 mm can be conducted to record the whole process of the test in real-time. Water and silicon oil were used as the pore and confining fluids, respectively. The normal and shear stresses were obtained by resolving the triaxial stress state onto the fracture plane [11]. In addition, the normal and shear stresses were corrected by considering the change in fractured con-

tact area and the deformation of Teflon drainage layers [12]. Fracture slip was computed by projecting the sample axial shortening onto the fracture direction.

2.2. Experimental Method and Program. Tests were conducted by adjusting the injection rate (IR) and fluid pressurization rate (PR) under different effective normal stress. The initial pore pressure (P_0) was set to 1 MPa. The shear strength at the onset of fault slip under constant pore pressure conditions, denoted τ_s , was determined by conducting an axial displacement loading test (Figure 2: stage1 (gray area)). Subsequently, we applied the shear stress τ_0 , equivalent to 93% of the shear strength, and fixed the normal stress (σ_n), assumed the fracture approaching a critical stress state (Figure 2: stage2 (yellow area)). Finally, the fluid pressure was applied from the bottom end of the sample by advancing the downstream syringe pump under constant effective normal stress (σ_{eff}) until a fracture slip occurred (Figure 2: stage3 (white area)). While the top end of the sample was connected to an intelligent digital pressure gauge, resulting in undrained boundary condition (Figure 1(b)). The fluid pressure in the top and bottom boreholes was monitored to observe fluid pressure distribution on the fracture. Note that confining pressure σ_3 remained constant throughout the fluid injection. We applied two different fluid injection schemes in the tests SW-1 and SW-2. The fluid pressure was increased stepwise from 1 to 7 MPa with a rate of 0.04 MPa/s in test SW-1 and 0.005 MPa/s in test SW-2 (Figure 3). Each fluid injection phase lasted for 8 min. For tests SW-1 and SW-2, fluid pressure was increased stepwise by 2 MPa, with each step lasting 1 and 7 min, respectively. Subsequently, the fluid pressure was held constant for 7 and 1 min for tests SW-1 and SW-2, respectively. In addition, three nonstepping injection-induced shear tests were carried out under 10 MPa, 20 MPa, and 26 MPa effective normal stresses, respectively. The experiment program is depicted in Table 1.

3. Experimental Results

3.1. The Role of Fluid Pressurization Rate. As shown in Figure 2(a) and Figure 2(b), the shear stress on the fracture surface showed a nearly linear increase during the initial

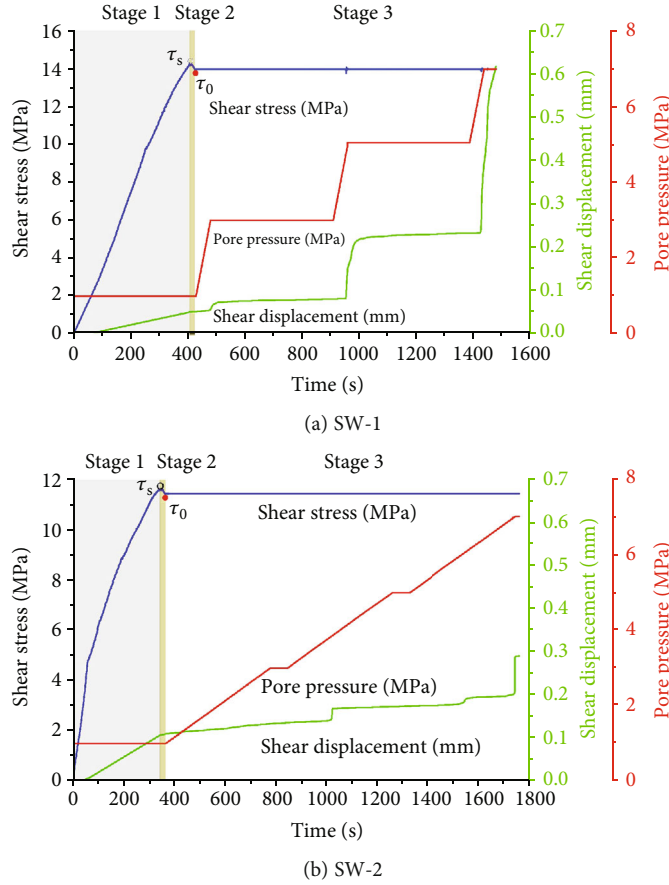


FIGURE 2: Stress-displacement evolution in stepping injection-induced shear tests. Please notice the difference in the coordinate scale.

loading stage (stage1), and the fracture slip rate gradually accelerated. Under $\sigma_n = 27$ MPa and $P_0 = 1$ MPa, the peak shear strength (τ_s) of tests SW-1 and SW-2 are very close ($\tau_s \approx 14$ MPa, $\tau_s \approx 12$ MPa), and then, the peak shear strength (τ_s) is reduced to about $0.93 \times \tau_s$ before injection. In the test SW-1, the saw-cut samples with critical stress begin to slip approximately at the end of the first fluid injection phase ($P_0 \approx 3.0$ MPa), slight slip hysteresis was detected, and there is no further slip during the pressure holding phase. This indicates that the magnitude of fluid pressure may control the onset of fracture slip. At a relatively fast fluid pressurization rate, slow stick-slip events were observed (slow stick-slip events are defined as peak slip speeds of less than 1 mm/s). Slip abruptly accelerated to peak velocity and then decelerated slowly. Subsequently, a slight hysteresis slipping of the fracture was induced at the end of each fluid pressurization phase. By contrast, in the test SW-2, saw-cut samples with critical stress did not show significant slip after the first fluid injection phase ($P_0 \approx 3.0$ MPa). Instead, it shows a significant slipping hysteresis, which may be due to the combined action of fluid pressure heterogeneity and fracture surface permeability evolution. In addition, compared with the test SW-1, fluid injection rate is 8 times slower, almost continuous fracture creep was observed, which indicates that the fluid pressurization rate may control the fracture slip mode.

3.2. *Deformation Characteristics of Fracture during Fluid Injection.* As shown in Figures 2(a) and 2(b), the shear displacement increases gradually at each stage of fluid injection. One aspect, the shear creep behavior occurs under constant shear stress, resulting in an increase in shear displacement. The other aspect, fluid injection reduces the effective normal stress and frictional resistance, so the fracture is more likely to slip as the shear displacement increases. In the test SW-1, episodic slow stick-slip events were observed, the slipping speed is less than $2 \mu\text{m/s}$ for long slipping duration of 60 seconds or more. In the SW-2, the slip at the low-pressure rate is apparently intermittent, and a number of small slips accumulate leading to eventual instability. But the slipping speed increases with the maximum $< 0.2 \mu\text{m/s}$ while slowly increasing and decreasing. Seismic (unstable) slip for natural faults generally shows high slip velocities (≥ 0.1 m/s) [13]. Thus, in these experiments, fluid pressure may promote steady and slow slipping [14–16]. It can also be seen that the fracture does not expand significantly during the initial injection stage. With the increase of injection pressure, fracture expansion occurred and gradually accelerated, indicating that fracture opening occurred during the slipping process. This condition may reflect surface roughness and associated shear dilation under the combined action of shear stress and continuous injection [17]. After that, the rate of expansion

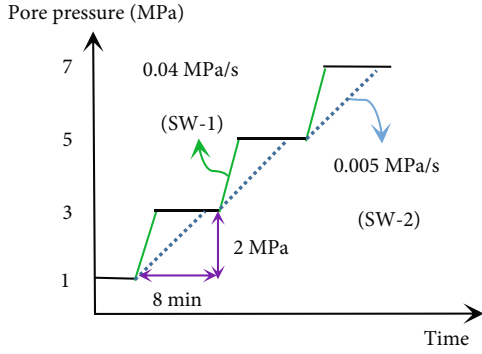


FIGURE 3: Stepping injection process.

TABLE 1: Experimental program and parameter setting.

| Test no. | σ_n (MPa) | P_0 (MPa) | σ_{eff} (MPa) | IR (MPa/s) |
|----------|------------------|-------------|-----------------------------|------------|
| SW-1 | 27 | 1 | 26 | 0.04 |
| SW-2 | 27 | 1 | 26 | 0.005 |
| T-1 | 11 | 1 | 10 | 0.005 |
| T-2 | 21 | 1 | 20 | 0.005 |
| T-3 | 27 | 1 | 26 | 0.005 |

increased dramatically. When the fracture is activated, the shear displacement remains stable at the current position due to a combination of reduced injection pressure and shear creep behavior. However, when the injection pressure is unloaded, the fracture tends to close. The normal displacement recovery also has the hysteresis phenomenon. Therefore, in this case, injection-induced fracture activation can be well characterized by the mechanism of deformation.

3.3. Influence of Fluid Pressure Heterogeneity. In order to study the influence of fluid pressure heterogeneity on fault slip, three tests were carried out at a water injection rate of 0.005 MPa/s under an effective normal stress of 10 MPa, 20 MPa, and 26 MPa, respectively. As shown in Figures 4(a)–4(c), the Mohr-Coulomb failure envelope was constructed by shear strength (Figure 4(d); solid red circle), and the friction coefficient μ was 0.62.

As shown in Figure 4(d), the stress state of the saw-cut fracture is represented by a solid green five-pointed star, which is located below the Mohr failure envelope. When loaded at a constant fluid rate, the effective normal stress gradually decreases until the fracture slips unsteadily (solid pink five-pointed star). Obviously, the measured fluid pressure in the water injection hole is greater than that predicted by the failure criterion. The deviation between them increases with the increase of effective normal stress and water injection rate. Through analysis, we believe that when the effective normal stress and fluid injection rate are high, the compression of fracture aperture becomes smaller and the fracture surface permeability increases, which leads to the amplification of the heterogeneity of fluid pressure. In order to verify the analysis results, the Coulomb failure stress change ($\mu\Delta P$) can be obtained from equation (1) [18], which is caused by the change of pore pressure. The calculated cou-

lomb stress at the beginning of fracture slipping is about one time larger than that predicted by the failure criterion. The increment of Coulomb fracture stress value is greater than 1.65 MPa during each test process of fluid injection-induced fracture instability. It fully shows that the cause of fracture instability is related to the variation of Coulomb fracture stress caused by pore pressure, and the influence is amplified by the fluid pressure heterogeneity.

$$\Delta\text{CFS} = \Delta\tau - \mu\Delta\sigma_{\text{eff}}, \quad (1)$$

where ΔCFS is the variation of Coulomb fracture stress, $\Delta\tau$ is the variation of shear stress, μ is the friction coefficient, and $\Delta\sigma_{\text{eff}}$ is the effective normal stress.

3.4. Influence of Permeability Changes. In order to study the influence of permeability evolution on fracture instability, the cubic law is used to calculate the permeability K_m (m^2) on the fracture surface (equations (2) and (3)) [19, 20].

$$b_m = - \left(\frac{12\eta \cdot L(t) \cdot Q(t)}{W \cdot \Delta P} \right)^{\frac{1}{3}}, \quad (2)$$

$$K_m = \frac{b_m^2}{12}, \quad (3)$$

where b_m (m) is the averaged hydraulic aperture, η (Pa·s) is the viscosity of fluid, $L(t)$ (m) is the contact length of the fracture surface, W (m) is the fracture width, $Q(t)$ (m^3/s) is the measured flow rate, and ΔP (Pa) is the differential pressure between the upstream and downstream extent of the fracture.

Figure 5 shows the variation of the friction coefficient and permeability on the fracture surface with slipping displacement and pore pressure at different fluid pressurization rates. In the test SW-1, when the fluid pressurization rate is high, the friction coefficient increases almost linearly with the increase of slipping displacement and, then, remains relatively stable after reaching the peak value, while the permeability of the fracture surface decreases almost linearly (Figure 5(a)). Compared with the test SW-1, the permeability of the fracture surface decreases relatively slowly and the average permeability is higher with the increase of the slipping displacement in test SW-2. When the slip displacements are 0.55 mm and 0.7 mm, respectively, the permeability is hysteresis and beyond the fracture slipping initial point of the second and third stages and, suddenly, decreases. The friction coefficient gradually increased to a peak during the stage1 of fluid injection and then decreased, until remained relatively stable (Figure 5(b)). The reduction of fracture surface permeability may be due to roughness degradation. Due to shear expansion, a sudden increase in the slipping rate temporarily increases the fracture permeability, but as the wear products fill the pore space, the permeability decreases with the increase of the slipping displacement. In addition, Figures 5(c) and 5(d) also show the change of friction coefficient and permeability with the increase of pore pressure. In SW-1 test, the permeability increases linearly and slowly with pore pressure until it suddenly increases at 3 MPa and 5 MPa

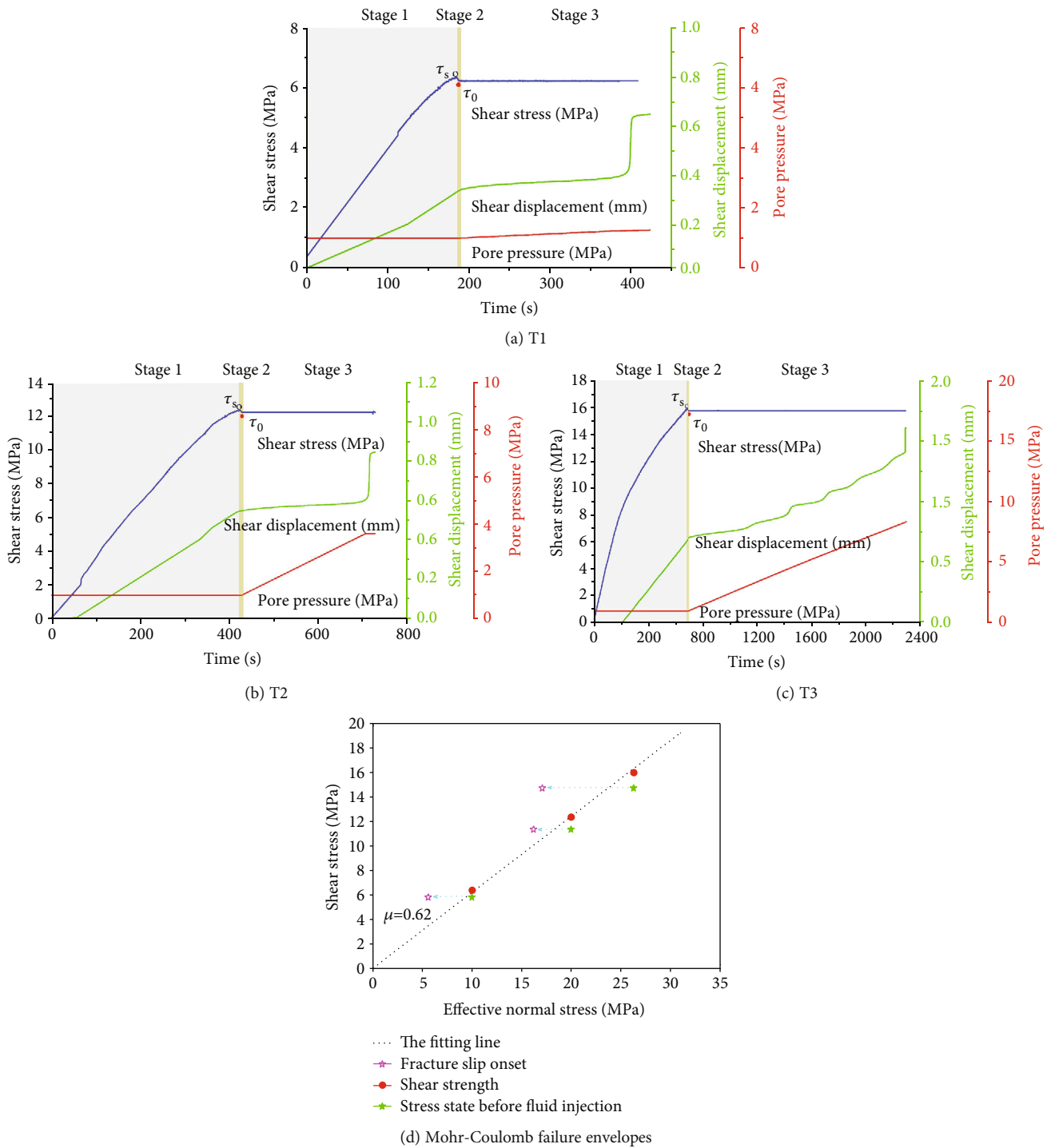


FIGURE 4: Stress-displacement evolution in nonstepping injection-induced shear tests. (a–c) Tests T1, T2, and T3. (d) Mohr-Coulomb failure envelopes obtained by fitting the shear strengths (solid red circle) from the displacement-driven shear tests, and the stress states of sawcut fractures before the fluid injection (solid green five-pointed star) and at the onset of injection-driven fracture instability (solid pink five-pointed star). Please notice the difference in the coordinate scale.

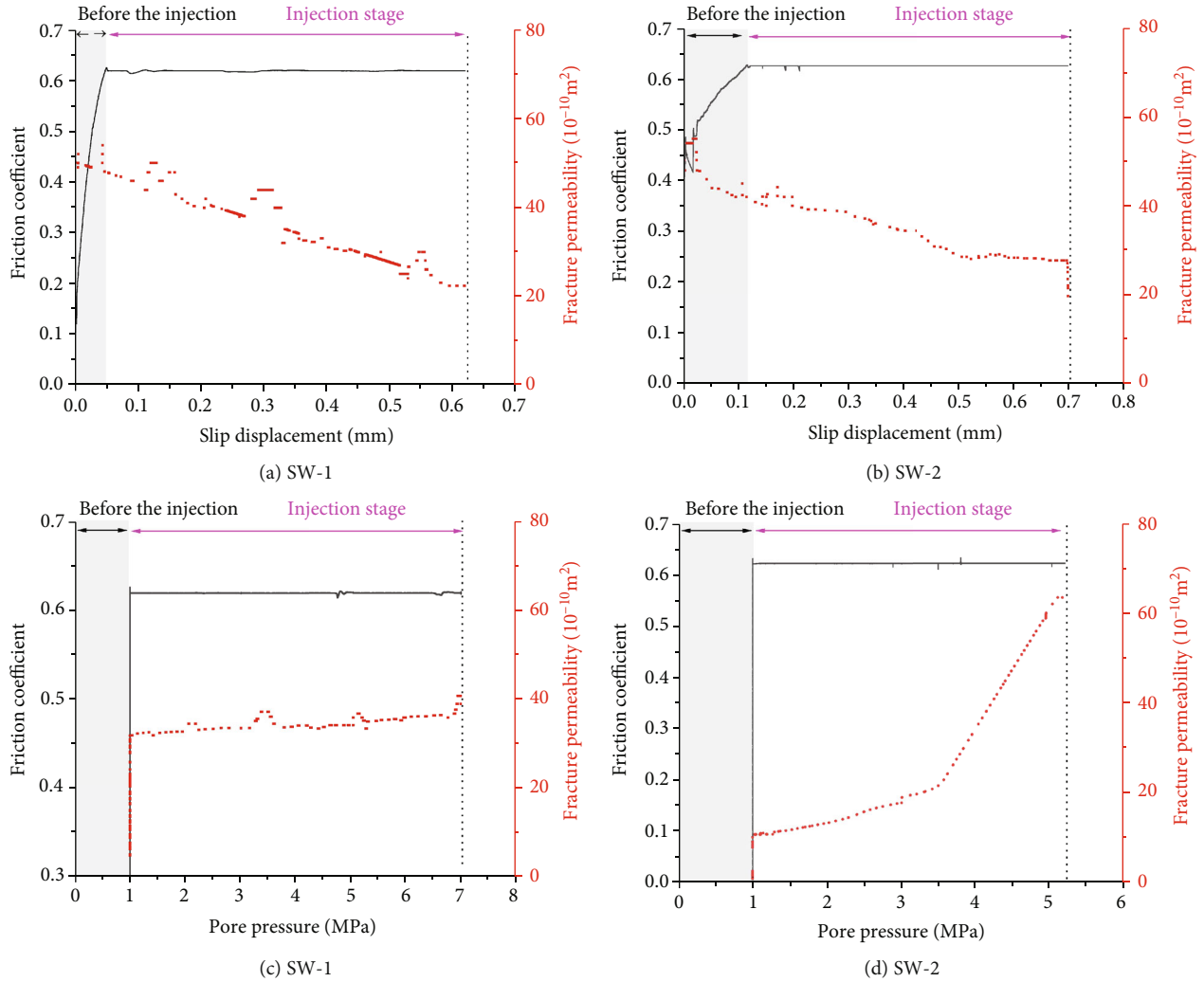


FIGURE 5: Friction coefficient and permeability evolution. (a, b) The friction coefficient and fracture surface permeability in SW-1 and SW-2 tests as functions of slip displacement, respectively. (c, d) The friction coefficient and fracture surface permeability as a function of pore pressure in SW-1 and SW-2 tests, respectively.

and, then, continues to grow slowly and relatively steadily. Slight infiltration lag was detected during injection pressure loading and holding. In contrast, in test SW-2, the permeability increased rapidly throughout the injection process, and there was no obvious sudden increase at 3 MPa and 5 MPa. However, significant permeability hysteresis was detected during injection pressure loading and holding stages.

In view of the above experimental phenomenon, when the fluid pressurization rate is small, the permeability increases rapidly with the increase of fluid pressure and decreases slowly with the increase of slipping displacement. This results in the fracture surface being able to maintain relatively high average permeability and weak fluid pressure heterogeneity. On the contrary, when the fluid pressurization rate is high, the permeability increases slowly with the increase of fluid pressure and decreases rapidly with the increase of slipping displacement. This results in the fracture surface being able to maintain relatively low average permeability and strong fluid pressure heterogeneity. Note that we

are studying the entire process of fracture slipping, not the local features.

4. Conclusions

In order to understand the influence of fluid pressurization rate on rock fracture slip, a series of injection-induced shear tests were carried out. The influence of fluid pressurization rate on fracture slip mode and displacement evolution process under different fluid injection rates is compared and analyzed. Then, we aim at the phenomenon of fracture slipping hysteresis at fluid pressurization rate; further analysis is made from two aspects of fluid pressure heterogeneity and permeability evolution. The main conclusions are summarized as follows:

- (1) The magnitude of fluid pressure may control the initiation of fracture slip, while the fluid pressurization rate may control the fracture slip mode. The fracture exhibits a slow stick-slip mode at a relatively fast fluid

pressurization rate, whereas the fracture exhibits an almost continuous creep mode at a relatively slow fluid pressurization rate

- (2) The contribution of fluid pressure heterogeneity and permeability evolution to fracture slip initiation is different with the increase of fluid pressurization rate. Under low fluid pressurization rate, fracture slipping shows obvious hysteresis phenomenon, which may be caused by the combined action of fluid pressure heterogeneity and permeability evolution. When the fluid pressurization rate is low, the fluid pressure heterogeneity is weak, and the permeability growth rate is fast. The influence of permeability on fracture slipping initiation may be more significant than the fluid pressure heterogeneity. With the increase of fluid pressurization rate, the fluid pressure heterogeneity may play a more significant role than permeability. This provides a supplementary insight for revealing the mechanism of seismogenic time lag behind fluid injection time
- (3) Under the experimental scale, the Coulomb fracture stress at the initiation of fracture instability is magnified by about one time than that predicted by the failure criterion due to the fluid pressure heterogeneity. In addition, the increment of Coulomb fracture stress during the test is greater than 1.65 MPa, which indicates that the heterogeneity of fluid pressure is closely related to fracture slip, and the increment of Coulomb fracture stress value greater than 1.65 MPa may be detrimental to fracture stability

Data Availability

For more information regarding the data availability, please reach out to the corresponding author.

Conflicts of Interest

The authors declare no conflict of interest.

Acknowledgments

This research was funded by the Special Fund for Formation and Evolution of Reservoir Fracture Networks, grant number Y411708117.

References

- [1] G. M. Atkinson, D. W. Eaton, and N. Igonin, "Developments in understanding seismicity triggered by hydraulic fracturing," *Nature Reviews Earth & Environment*, vol. 1, no. 5, pp. 264–277, 2020.
- [2] W. L. Ellsworth, "Injection-induced earthquakes," *Science*, vol. 341, no. 6142, article 1225942, 2013.
- [3] Y. Ji, W. A. M. Wanniarachchi, and W. Wu, "Effect of fluid pressure heterogeneity on injection-induced fracture activation," *Computers and Geotechnics*, vol. 123, article 103589, 2020.
- [4] A. A. Holland, "Earthquakes triggered by hydraulic fracturing in south-central Oklahoma," *Bulletin of the Seismological Society of America*, vol. 103, no. 3, pp. 1784–1792, 2013.
- [5] Y. Wang, W. K. Feng, R. L. Hu, and C. H. Li, "Fracture evolution and energy characteristics during marble failure under tri-axial fatigue cyclic and confining pressure unloading (FC-CPU) conditions," *Rock Mechanics and Rock Engineering*, vol. 54, no. 2, pp. 799–818, 2021.
- [6] M. Kozłowska, M. R. Brudzinski, P. Friberg, R. J. Skoumal, N. D. Baxter, and B. S. Currie, "Maturity of nearby faults influences seismic hazard from hydraulic fracturing," *Proceedings of the National Academy of Sciences*, vol. 115, no. 8, pp. E1720–E1729, 2018.
- [7] L. Wang, G. Kwiatek, E. Rybacki, M. Bohnhoff, and G. Dresen, "Injection-induced seismic moment release and laboratory fault slip: implications for fluid-induced seismicity," *Geophysical Research Letters*, vol. 47, no. 22, pp. 1–11, 2020.
- [8] Y. Ji and W. Wu, "Injection-driven fracture instability in granite: mechanism and implications," *Tectonophysics*, vol. 791, pp. 1–12, 2020.
- [9] C. Noël, F. X. Passelègue, C. Giorgetti, and M. Violay, "Fault reactivation during fluid pressure oscillations: transition from stable to unstable slip," *Journal of Geophysical Research: Solid Earth*, vol. 124, no. 11, pp. 10940–10953, 2019.
- [10] F. X. Passelègue, N. Brantut, and T. M. Mitchell, "Fault reactivation by fluid injection: controls from stress state and injection rate," *Geophysical Research Letters*, vol. 45, no. 23, pp. 12837–12846, 2018.
- [11] J. C. Jaeger, N. G. Cook, and R. Zimmerman, *Fundamentals of Rock Mechanics*, John Wiley & Sons, Oxford, UK, 2009.
- [12] A. H. Kohli and M. D. Zoback, "Frictional properties of shale reservoir rocks," *Journal of Geophysical Research: Solid Earth*, vol. 118, no. 9, pp. 5109–5125, 2013.
- [13] R. Bürgmann, "The geophysics, geology and mechanics of slow fault slip," *Earth and Planetary Science Letters*, vol. 495, pp. 112–134, 2018.
- [14] F. Cappa, M. M. Scuderi, C. Collettini, Y. Guglielmi, and J. P. Avouac, "Stabilization of fault slip by fluid injection in the laboratory and in situ," *Science Advances*, vol. 5, pp. 1–8, 2019.
- [15] M. E. French, W. Zhu, and J. Banker, "Fault slip controlled by stress path and fluid pressurization rate," *Geophysical Research Letters*, vol. 43, no. 9, pp. 4330–4339, 2016.
- [16] Y. Wang, Y. F. Yi, C. H. Li, and J. Q. Han, "Anisotropic fracture and energy characteristics of a Tibet marble exposed to multi-level constant-amplitude (MLCA) cyclic loads: a lab-scale testing," *Engineering Fracture Mechanics*, vol. 244, article 107550, 2021.
- [17] B. Derode, Y. Guglielmi, L. De Barros, and F. Cappa, "Seismic responses to fluid pressure perturbations in a slipping fault," *Geophysical Research Letters*, vol. 42, no. 9, pp. 3197–3203, 2015.
- [18] X. Lei, G. Yu, S. Ma, X. Wen, and Q. Wang, "Earthquakes induced by water injection at ~3 km depth within the Rongchang gas field, Chongqing, China," *Journal of Geophysical Research: Solid Earth*, vol. 113, no. B10, pp. 1–12, 2008.
- [19] F. Cappa, Y. Guglielmi, C. Nussbaum, and J. Birkholzer, "On the relationship between fault permeability increases, induced stress perturbation, and the growth of aseismic slip during

fluid injection,” *Geophysical Research Letters*, vol. 45, no. 20, pp. 11012–11020, 2018.

- [20] Z. Ye and A. Ghassemi, “Injection-induced shear slip and permeability enhancement in granite fractures,” *Journal of Geophysical Research: Solid Earth*, vol. 123, no. 10, pp. 9009–9032, 2018.